Journal of Electronic Materials (2025) 54:6685–6700
https://doi.org/10.1007/s11664-025-12036-w

ORIGINAL RESEARCH ARTICLE

Simulation-Driven Insights into the Structural, Electronic, and Optical Properties of x:CdS (x = Mg, Ca, and Sr) for Enhanced Optoelectronic Performance

Mosfiqur Rahman[1,2] · Mst. Afroza Akter[3] · Md. Mamunur Roshid[4,5] · Md. Monirul Haq[2]

Received: 6 March 2025 / Accepted: 28 April 2025 / Published online: 31 May 2025

Abstract

Zinc blende cadmium sulfide (CdS), a direct bandgap II–VI semiconductor holds immense potential for optoelectronic applications. However, challenges such as limited light absorption and stability often hinder its performance. This study, employing density functional theory (DFT) via CASTEP, investigates the effects of alkaline earth metals doping on the structural, electronic, and optical properties of CdS. Doping modifies lattice constants and bond lengths, resulting in notable bandgap enhancements: Mg (1.331 eV), Ca (1.399 eV), and Sr (1.366 eV), attributed to the Burstein–Moss effect. Optical analyses reveal enhanced dielectric constants, with static values increasing to 5.14 (Mg), 4.88 (Ca), and 4.34 (Sr) compared to 4.56, the dielectric constant of undoped CdS. Elevated absorption across the UV-visible spectrum and shifts in photoconductivity peaks to higher energy regions underscore their capacity for superior light interaction. Moreover, photoconductivity and dielectric loss analyses highlight Mg's pronounced impact on carrier dynamics. These findings demonstrate that alkaline earth metal doping effectively tailors CdS for advanced optoelectronic applications, providing a pathway to high-performance semiconductors in energy and light technologies.

Keywords Cadmium sulfide (CdS) · density functional theory (DFT) · optoelectronic properties · doping effects (Mg, Ca, Sr) · bandgap engineering

Introduction

The III–V and II–VI semiconductor families include widely studied materials in electronics, optoelectronics, and spintronics.[1–4] Among these, II–VI semiconductors have gained attention due to their applications in modern technologies, particularly in photonics, light sensing, and device fabrication. Their relevance spans solar cells, light detection, x-ray detection, and photovoltaics.[5] II–VI semiconductors offer a broad bandgap range, from infrared to ultraviolet, making them ideal for optoelectronic and gas sensing applications. ZnTe, ZnS, and CdTe exhibit wide bandgaps, while HgTe and HgSe have narrower ones. Zinc blende cadmium sulfide (CdS) is a significant semiconductor due to its direct bandgap, stability, and optical transmittance, making it valuable for solar cells, photodetectors, LEDs, photocatalysis, and gas sensors.[6–8] However, its limited visible light absorption, poor charge carrier separation, and stability issues hinder its optoelectronic efficiency.[9,10] Doping is a promising method to overcome these limitations by modifying its structural, electronic, and optical properties.

CdS, an *n*-type II–VI semiconductor,[11] finds applications in nanotechnology,[5] visible light detection, and heterojunction solar cells.[12] It contributes to biosensing devices,[13,14] photo electroluminescent displays,[15] thin-film transistors,[16] gas detectors,[17] vacuum UV lenses,[18] LEDs,[5,19,20] photoelectrochemical solar cells,[21–23] and photovoltaics.[24] CdS exists

✉ Mosfiqur Rahman
mosfiqur56@gmail.com

1 Department of Physics, Uttara University, Holding 77, Beribadh Road, Turag, Dhaka, Uttara 1230, Bangladesh

2 Department of Physics, Begum Rokeya University Rangpur, Rangpur 5400, Bangladesh

3 Department of Applied Chemistry and Chemical Engineering, University of Dhaka, Dhaka 1000, Bangladesh

4 Department of Textile Engineering, Uttara University, Holding 77, Beribadh Road, Turag, Dhaka, Uttara 1230, Bangladesh

5 Department of Mathematics, Hamdard University Bangladesh, Hamdard Nagar, Gazaria, Munshiganj 1510, Bangladesh

in zinc blende, wurtzite, and rock salt structures, with the nanocrystalline rock salt phase being particularly stable and significant for semiconductor physics.[25–28] CdS nanostructures such as nanodots, nanorods, and nanowires serve roles in photonic switching, optoelectronics, photovoltaic cells, biolabeling, and bioimaging.[29,30]Khan et al. extensively studied CdS due to its emerging applications.[30,31]

CdS thin films are synthesized using spray pyrolysis,[32] vacuum deposition, electrodeposition, pulse laser deposition, chemical vapor deposition, thermal evaporation, sputtering, sol–gel spin coating, and chemical bath deposition.[33–35] Recent studies have successfully grown low-dimensional CdS structures. Ashwaq et al.[8] synthesized pure and (Co-Sr) co-doped CdS nanostructures using sol–gel spin coating. Gandouzi et al.[7] investigated Zn and (Zn-Ni) co-doped CdS thin films, revealing hexagonal nanostructures and bandgaps between 2.30 eV and 2.49 eV. DFT calculations confirmed an increased bandgap of 2.85 eV and a stable ferromagnetic state. AL-Jawad et al.[36] synthesized Mn-doped CdS nanoflower thin films using hydrothermal methods. Meysam et al.[37] prepared CdS nanocrystals (10–20 nm) via chemical bath deposition, while Prabakar et al.[38] developed CdS quantum dots on TiO_2 for improved solar cell efficiency. Studies have also explored doping with Na, Mg, Ni, Cu, Ag, and Pb, using various techniques.[39–42]

Doping influences CdS properties, leading to novel applications. Anbarsai et al. investigated Pb-doped CdS using spray techniques, observing red- and blueshifts, increased optical transparency, and decreased electrical resistivity[43]. Khan et al. confirmed similar trends through DFT studies, indicating enhanced optical absorption and optoelectrical properties for solar cells and photodetectors[44]. Heiba et al. synthesized $Cd_{0.9}Mg_{0.05}S$ via thermolysis, revealing two-phase CdS structures. UV-Vis and photoluminescence studies demonstrated Mg doping effects on bandgaps and photoluminescence intensities, while DFT calculations showed non-magnetic behavior[45]. Feng et al. synthesized Mg-doped CdS nanorods via solvothermal methods, showing increased bandgaps and improved photocatalytic degradation of RhB.[46] Chakraborty et al. developed Ca-doped CdS nanoparticles with rapid ethanol sensing (1-s response, 500-ppb detection limit), making them suitable for breath analyzers.[47]

Veerathangam et al. used SILAR methods to study Pb-doped CdS quantum dot solar cells, achieving a high power conversion efficiency.[32] Banerjee et al. examined Pb-doped nanostructured CdS films using XRD and UV-Vis spectroscopy.[48] Gutiérrez et al. performed chemical bath deposition of CdS:Pb^{2+} nanocrystals, observing blueshifts and improved crystallinity.[49] Al-Jumaili analyzed PbCdS thin films using XRD, AFM, SEM, and UV-Vis spectroscopy, confirming their suitability for photodetectors and solar cells.[50]

Khan et al. noted enhanced optical properties in Na:CdS thin films prepared by spin coating.[39] Ertis et al. demonstrated efficient visible-light photocatalysis in metal-doped CdS (Ni, Co, Ce, Sb) for methylene blue degradation.[51] Abuhusain et al. explored (Co-Sr) co-doped CdS, revealing ferromagnetic behavior and redshifts in band structures.[8]

Theoretical DFT studies on pure CdS have used various functionals, including LDA, PBE-GGA, and hybrid methods. Edossa et al.[7] analyzed CdS optoelectronic properties in zinc blende and wurtzite phases using LDA,[52] PBE,[53] GGA,[54] GGA + U,[55] and PBE0 hybrid functionals in Quantum Espresso,[56] finding that PBE0 best matched experimental data. Liu et al. investigated Cu-doped CdS defects using CASTEP, identifying their influence on ferromagnetic stability and optical properties.[57] Studies on B, Al, Ga, or In doping found Fermi level shifts and visible region absorption peaks.[58]

Doping also affects electronic and magnetic properties. Boudjelal et al. used DFT to study co-doped CdS, identifying ferromagnetic half-semiconductor gaps. [59] Sukkabot analyzed Mn-, Fe-, and Cu-doped CdS using spin-polarized DFT, noting semiconductor-to-metallic transitions.[60] Nabi examined Mn-doped CdS with Wien2k, confirming these findings[61].

Despite extensive experimental studies on Pb-doped CdS, theoretical studies using Wien2K, VASP, or CASTEP remain limited, particularly for zinc blende CdS. This gap motivated the present study, which investigates the optical and electronic properties of undoped and Mg-, Ca-, and Sr-doped CdS using CASTEP. Using PBE-GGA within DFT, we calculated the optical absorption, reflectivity, conductivity, extinction coefficient, refractive index, and dielectric constant. Additionally, TDOS and PDOS analyses provided insights into electronic behaviors. Our results align well with existing literature, contributing to the understanding of Mg-, Ca-, and Sr-doped CdS for optoelectronic and photoconductive applications.

Computational Methodology

In this study, first-principles calculations were carried out using the Cambridge Serial Total Energy Package (CASTEP) code[62] to carry out the electronic band structure, density of states (DOS), partial density of states (PDOS), and optical properties of undoped CdS and x: CdS (x = Mg, Ca, and Sr). Within the framework of density functional theory (DFT) with the generalized gradient approximation (GGA), Perdew–Burke–Ernzerhof (PBE) as an exchange–correlation functional[53] has been employed. The coupling between ions and electrons was simulated by ultrasoft pseudopotentials for Cd, S, Mg, Ca, and Sr atoms. The effect of spin-orbit interaction has been neglected. The valence electron configurations

of Cd, S, Mg, Ca, and Sr atoms were considered as $4d^{10}5s^2$, $3s^23p^4$, $2p^63s^2$, $3s^23p^64s^2$, and $4s^24p^65s^2$, respectively.

CdS is a symmetry system possessing the space group of $F\bar{4}3m$ with a face-centered cubic (FCC) structure and belongs to a member of 216. Four Cd-cations and four S-anions make up the unit cell. Thus, the CdS crystal can be characterized as a series of Cd–S double layers stacked along the *a*-axis or (100) directions. The lattice parameters are the second nearest-neighbor distances $a = b = c = 5.83$ Å and $\alpha = \beta = \gamma = 90°$,[63] and the CdS bond length along the direction of all the axes is 2.524 Å. In order to calculate all the parameters of the undoped and x:CdS (x = Mg, Ca, and Sr) $2 \times 1 \times 1$ supercells, the Brillouin zone (BZ) was sampled employing the plane-wave cut-off energy of 400 eV and the $5 \times 5 \times 5$ Monkhorst–Pack grid. All the calculations have been performed in reciprocal space with a careful convergence criterion to ensure the reliability of the results. The maximum force was set to 0.05 eV $Å^{-1}$, and maximum stress was at 0.10 GPa. The total energy was converged to within 2×10^{-5} eV/atom, and the geometry optimization has been performed with high precision to minimize the error in the computed results. The computational efficiency was maximized by employing parallelization strategies on high-performance computing clusters, allowing for large-scale calculations on supercells with multiple dopant configurations. We take into account a cell larger than the fundamental unit in order to analyze the fractional Mg, Ca, or Sr atom substitution.

The zinc blende phase of CdS was chosen as the host material, with a $2 \times 1 \times 1$ supercell containing 16 atoms (8 Cd and 8 S atoms), as seen in Fig. 1a, b, c, and d. To simulate the doping effects, one Cd atom in the CdS supercell is substituted with Mg, Ca, or Sr atoms one after another, maintaining a fixed dopant concentration to study the impact on the material's properties. The doping concentration was chosen such that it ensures a consistent analysis of the modifications induced by each dopant. All DFT calculations have been performed using GGA for the exchange–correlation functional, specifically the PBE functional, which is known for providing reliable results for semiconductors and transition metal compounds. The CASTEP module of Materials Studio has been employed for the DFT simulations due to its robust performance in electronic structure calculations, including its support for periodic boundary conditions and the plane-wave basis set approach.

In addition to the band structure calculations, to explore the effects of doping on the material's optical properties, the real and imaginary parts of the dielectric function have been computed by evaluating the transition matrix elements between Kohn–Sham states in the material's electronic structure. The refractive index and extinction coefficient were also calculated. These properties offer valuable insights into how the material interacts with light, including light propagation and scattering behaviors. The refractive index provides information about the material's ability to bend light, while the extinction coefficient describes how the material absorbs light at different wavelengths. The absorption coefficient has been calculated across a wide photon energy range, including the ultraviolet and visible regions, to assess how doping influences the optical absorption characteristics of CdS. This is important for applications in optoelectronic devices, as it helps to determine whether doping can enhance light absorption in the desired spectral range. Reflection spectrum measures the light reflected by a semiconductor, revealing optical properties. A drop at the bandgap indicates absorption, while interband transitions and free carriers affect reflectance. Photoconductivity is the increase in a semiconductor's conductivity under light exposure, as photons generate electron-hole pairs. It depends on bandgap energy, defects, carrier lifetime, and excitation wavelength, influencing applications like photodetectors and solar cells. The electron energy loss function, derived from the real and imaginary parts of the dielectric function, is used to understand the material's interaction with high-energy electrons.

In summary, this computational methodology combines advanced DFT calculations with a carefully constructed supercell model to explore the effects of Mg, Ca, and Sr doping on the structural, electronic, and optical properties of CdS. By utilizing the CASTEP module in Materials Studio, the study provides a comprehensive analysis of the doping-induced modifications in CdS, offering insights that can be used to enhance its performance in optoelectronic applications such as solar cells, photodetectors, and light-emitting devices.

Results and Discussion

Geometry Optimization and Structural Properties

The CdS is a zinc blende crystal structure having space group $F\bar{4}3m$ is a face centered cubic (FCC) structure and belongs to a member 216 with Cd and S-atomic planes stacked along [111] direction illustrated in Fig. 1. First, in order to investigate how impurities influenced the stability of the structure during the calculation, the structure of pure and Mg-, Ca-, and Sr-doped CdS $2 \times 1 \times 1$ supercells were optimized. Following geometry optimization, the band structure and DOS were calculated. Table I lists the computed results for structural and electronic analysis and demonstrates the reliability of the computational methods. The obtained lattice constants are observed to be a bit larger than those for x:CdS (x = Mg, Ca, and Sr).

It is noteworthy that these assumptions differ by between 1% and 3% from the experimental values of lattice constant 5.83 Å,[64] which demonstrates that our calculations are

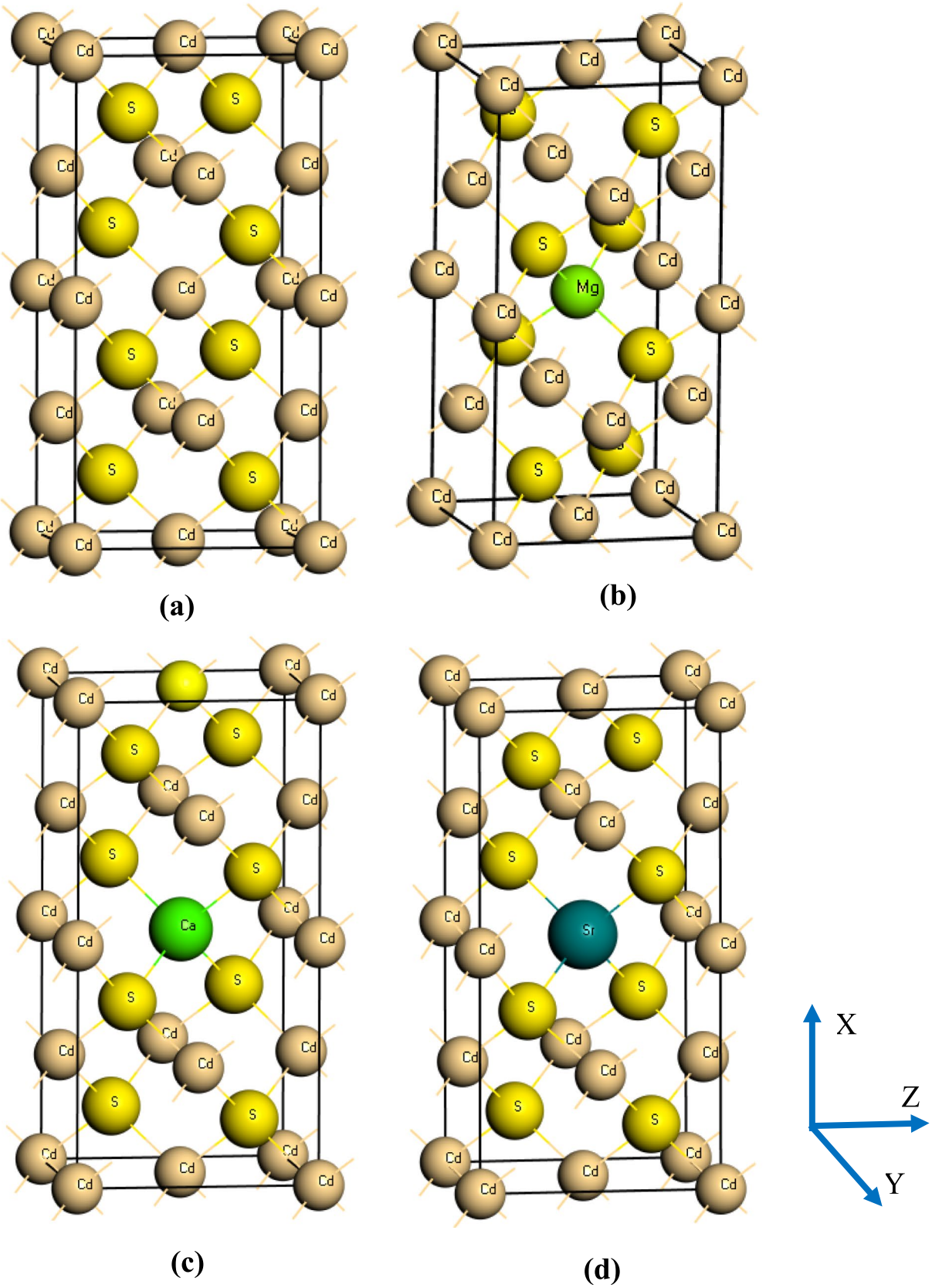

Fig.1 Optimized structures of (a) undoped, (b) Mg-doped CdS, (c) Ca-doped, and (d) Sr-doped CdS $2 \times 1 \times 1$ supercells.

Table I Structural and electronic parameters of undoped and x:CdS (x = Mg, Ca, and Sr) 2 × 1 × 1 supercells after geometry optimization

Sample's name	Lattice constants, a (Å)	Deviation (%)	Volume ($Å^3$)	Bandgap, E_g (eV)	Bond length (Å)		Bulk modulus, K (GPa)
CdS	5.950[a], 5.8[b], 5.82[c]	2.05	210.644	1.088[a], 1.08[e]	Cd–S	2.567[a], 2.64[f]	65.550
Mg:CdS	5.920[a], 5.8677[c]	1.54	207.474	1.331[a], 1.32[e]	Cd–S Mg–S	2.580 2.484	35.897
Ca:CdS	5.994[a]	2.81	215.352	1.399	Cd–S Ca–S	2.583 2.704	69.515
Sr:CdS	5.998[a]	2.88	215.784	1.366	Cd–S Sr–S	2.571 2.817	59.843

[a]Present work. [b]Ref. 64. [c]Ref. 66. [d]Ref. 45. [e]Ref. 46. [f]Ref. 5.

reasonable.[63] The calculated bond lengths among Cd, S, Mg, Ca, and Sr are Cd–S, Mg–S, Ca–S, and Sr–S bond lengths for pure and x:CdS (x = Mg, Ca, and Sr) are depicted in Table I which are marginally greater than that of the bulk CdS 2.524 Å.

The valence electron configurations of Cd, Mg, Ca, and Sr atoms were considered as $4d^{10}5s^2$, $2p^63s^2$, $3s^23p^64s^2$, and $4s^24p^65s^2$, respectively. The observed distortion in the lattice constant and bond lengths of CdS monolayer upon substituting Cd^{2+} with Mg^{2+}, Ca^{2+}, and Sr^{2+} atoms may be attributed to the different ionic radii of the Mg^{2+}, Ca^{2+}, and Sr^{2+} ions (0.72 Å, 1.00 Å, and 1.12 Å compared to the Cd^{2+} ion (0.97 Å).[65] Despite this size difference, the incorporation of Mg, Ca, and Sr atoms leads to notable distortions in the structure of the CdS monolayer. Consequently, the grain size tends to first decrease for Mg doping and then increase, suggesting that Mg, Ca, and Sr have a significant influence on the grain growth of CdS.[66] However, these variations in grain size can lead to a reduction in the material's mechanical strength and crystal hardening properties.[66] Moreover, the relaxed cubic structures (shown in Fig. 1a–d) indicate that the Cd–S bond length remains uniform, which is a result of the high symmetry within the geometry. Even with the substitution of Cd by Mg, Ca, and Sr atoms, the 2D configuration of the CdS monolayer is largely preserved, with only minor distortions observed.

Band Structure and Density of States (DOS)

The total density of states (TDOS) and partial density of states (PDOS) of undoped CdS and Mg-, Ca-, and Sr-doped CdS 2 × 1 × 1 supercells have been computed using the GGA functional approximation without spin-orbit interaction in order to achieve an extensive comprehension of the electronic structure. Along with the high symmetry lines G(0.0, 0.0, 0.0), F(0.0, 0.5, 0.0), Q(0.0, 0.5, 0.5), Z(0.0, 0.5, 0.5), and G(0.0, 0.0, 0.0), respectively, in the first Brillouin zone, the results of electronic band structures are shown in Fig. 2a–d. The conduction and valence bands are separated above and below the Fermi level (EF), which was set to zero. It is confirmed from Figs. 2(a–d) that the conduction band minimum (CBM) and the valence band maximum (VBM) are at the same k-point (G–G) indicating that the CdS is a direct bandgap semiconductor with an energy of 1.088 eV and is in good agreement based on DFT.[46] The calculated bandgap of Mg-doped CdS is 1.331 eV. These values are significantly lower than experimental results due to the inherent limitations of the GGA functional in first-principles calculations.[67] However, the bandgap of Mg-doped CdS is larger than that of CdS, consistent with experimental findings.[46] This suggests that Mg doping effectively widens the bandgap of CdS. A wider bandgap helps suppress the recombination of photogenerated carriers, thereby enhancing photocatalytic performance.

The obtained calculated value is smaller than the experimental value (2.42 eV).[45,65] It should be noted that the electronic bandgaps of semiconductors are grossly underestimated due to neglect of correlations between excited-state electrons is a well-known artifact of the traditional DFT.[68,69] For undoped CdS, and Mg-, Ca-, and Sr-doped CdS 2 × 1 × 1 supercells, the lowest and the highest values of bandgap are obtained at the same (G–G) points. In the case of a direct bandgap semiconductor, the excitation of electrons from the VBM to the CBM occurs at the lowest energy, hence, the bandgap of CdS is taken at the G–G point, where the excitation of electrons most probably occurred.

From Fig. 2b–d, the corresponding bandgaps of Mg-, Ca-, and Sr-doped CdS are 1.331 eV, 1.399 eV, and 1.366 eV, respectively, taken at the G–G point. The investigated bandgaps of Mg-, Ca-, and Sr-doped CdS are greater than that of undoped CdS (Fig. 2a). As Mg, Ca, and Sr are doped into CdS, the impurity energy level, i.e., the acceptor level, appears below the valence band and the Fermi level shifts upward into conduction band by 0.243 eV and 0.311 eV, and 0.278, respectively, for Mg-, Ca-, and Sr-doped CdS which can be related to the Burstein–Moss (BM) effect.[70] In this

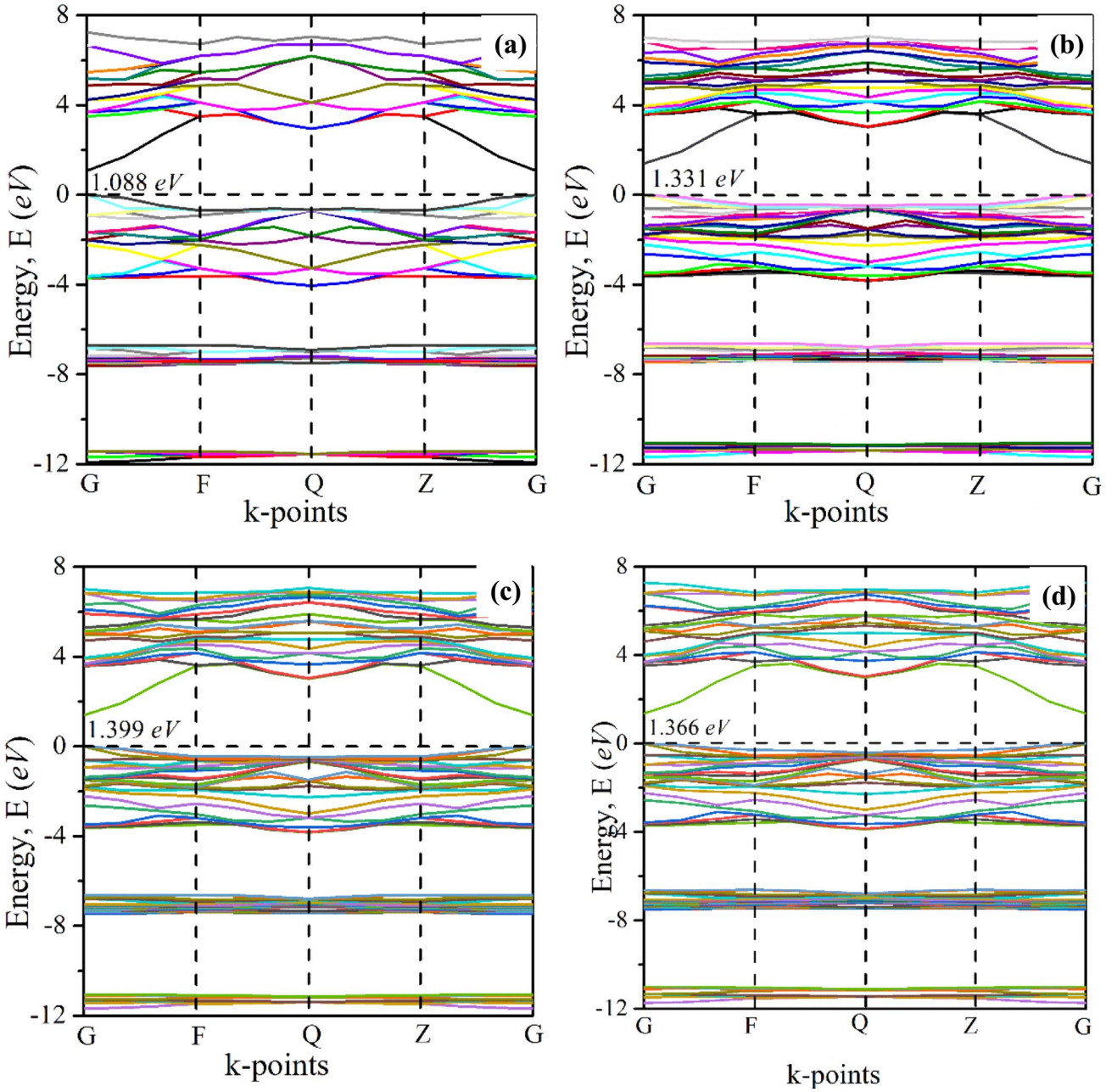

Fig. 2 Calculated band structures of (a) undoped, (b) Mg-doped CdS, (c) Ca-doped, and (d) Sr-doped CdS, 2 × 1 × 1 supercells.

case, holes can be excited easily from the impurity level to the valence band, causing an increase in the impurity carrier concentrations and enhancement of the conductivity. This reveals that the *p*-type CdS can be obtained by Mg, Ca, and Sr doping and may also achieve a high-quality and more stable *p*-type CdS[71] with Mg, Ca, and Sr doping content. This increase in bandgap may occur due to the upward shifting of the conduction band when Mg, Ca, and Sr are doped into CdS supercells, called the BM effect.[68,69]

The electronic distributions of undoped CdS and x:CdS (Mg, Ca, and Sr) 2 × 1 × 1 supercells in an energy spectrum are represented in Fig. 3a–d by the TDOS and PDOS. To elaborate on the atomic contribution to the band formation, the TDOS has been calculated for all atoms, and the PDOS for individual atoms, respectively. From Fig. 3a, it can be seen that the upper valence band is mainly composed of S-3*p* states. The lower valence band consists of a *d*–*p* hybridization coupling between the Cd-4*d* and S-3*p* states with small contributions of the S-3 *s* states. The conduction band is mainly composed of S-3*p* states with a small contributions of Cd-5 *s* and Cd-4*p* states. The upper valence band ranges from – 4.15 eV to

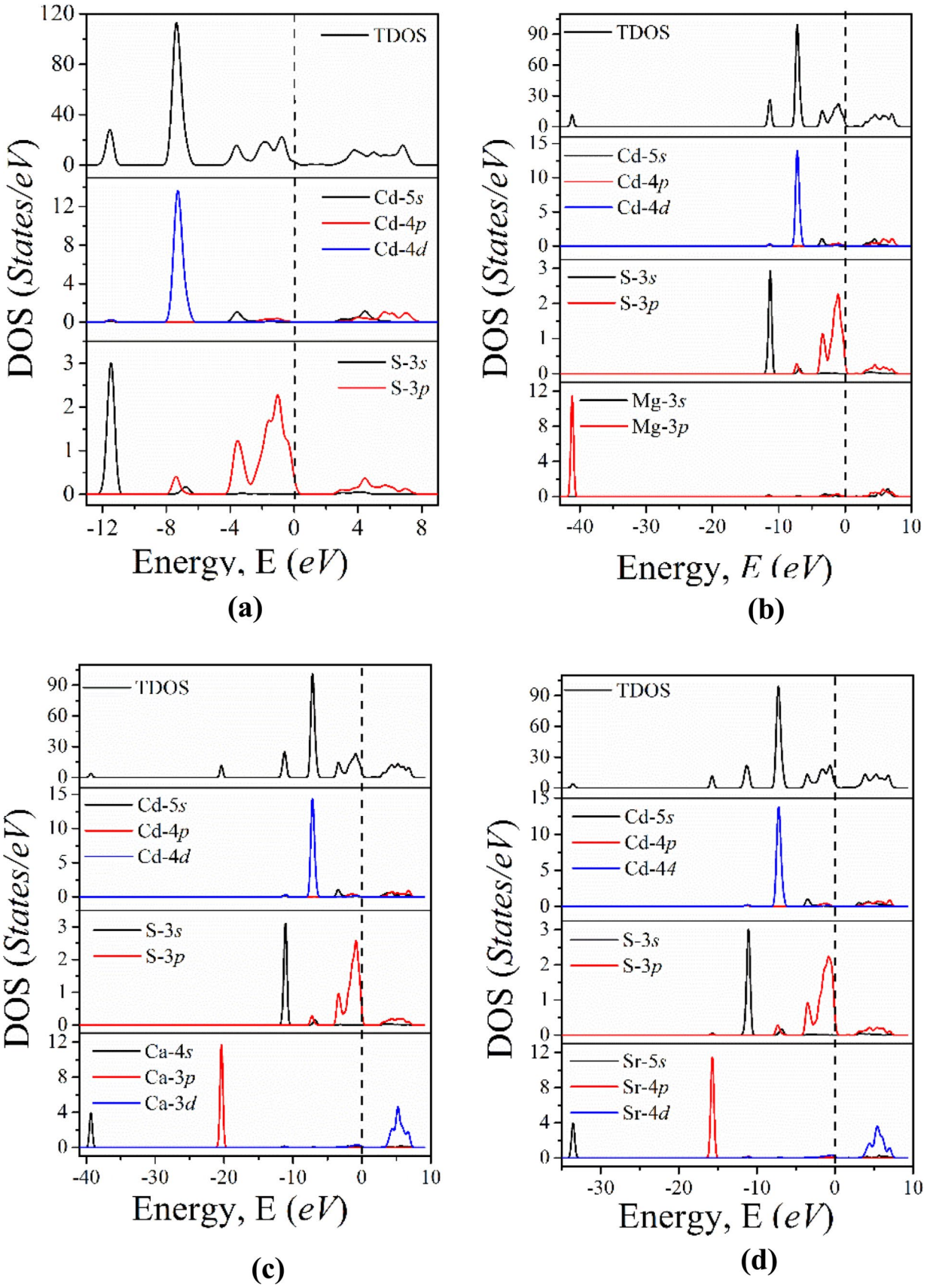

Fig. 3 Total and partial density of states of (a) undoped, (b) Mg-doped CdS, (c) Ca-doped, and (d) Sr-doped CdS, 2 × 1 × 1 supercells.

the Fermi level, and the lower valence band ranges from – 8.00 eV to – 4.15 eV.

The domination of S-3*p* to the valence band is located at − 1.02 eV. Simultaneously, Cd-4*p* states contribute a little to the conduction band, with an energy level of 5.63 eV. The core energy states spread between – 12.00 and – 8.00 eV, which originates only from the S-3 *s* states and is not considered in this work as its interaction with other electronic states is obscure . On the other hand, the calculated PDOS of the S atom has been dominated by the S-3 *s* states far beyond the Fermi level at – 11.48 eV. The valence band of the S atom is mainly contributed by the S-3*p* rather than the S-3 *s* states. In the conduction band, the S-3*p* and Cd-5 *s* are located above the Fermi level at an energy of 4.44 eV and make a *s–p* hybridization coupling between the Cd-5 *s* and S-3*p* states, which lie above the Fermi level. These results are in good agreement with other reports that have been characterized for pure CdS using first-principles calculations.[46]

The DOS and PDOS of x:CdS (x = Mg, Ca, and Sr) supercells are shown in Fig. 3b, c, revealing that the core state relating to Mg-3 *s* states in Mg-doped CdS, as well as Ca-4 s states and Sr-5 s states, contribute to the core-level density of states of Ca- and Sr-doped CdS, respectively. It is clear from Fig. 3b, c that the upper valence bands are completely dominated by the S-3*p* states, and the lower valence bands are occupied by the combination of the Cd-4*d* states and impurity atoms (Ca-3*p* and Sr-4*p*) states. At the conduction bands, the impurity peaks mainly come from the Mg-3 s and Mg-3p, Ca-3d, and Sr-4d states, shown by the PDOS of the Mg, Ca, and Sr atoms.

The DOS analysis shows that the impurity atoms (Mg, Ca, Sr) contribute negligibly to states above and below the Fermi level. This means the dopants do not introduce significant defect states that could lead to band tailing (which usually reduces the bandgap). Instead, they alter the band edges in a way that results in a larger separation between the CBM and the VBM. Also, Cd is more electronegative (1.69) than the impurity atom dopants, Mg (1.31), Ca (1.00), and Sr (0.95). In fact, when Cd is substituted with these dopants, the Cd–S bond is replaced with Mg–S, Ca–S, or Sr–S bonds, which are less covalent and more ionic in nature. This reduces the interaction of the dopant's orbitals with the host material, decreasing the contribution of impurity states near the valence and conduction bands, effectively widening the bandgap. Also, the ionic radii of Mg^{2+} (0.72 Å) < Ca^{2+} (1.00 Å) < Sr^{2+} (1.12 Å),[65] all of which are larger than Cd^{2+} (0.97 Å).[65] As larger atoms replace Cd, there could be minor lattice distortions, affecting the crystal field and altering the electronic band structure. In some cases, such distortions reduce the overlap of atomic orbitals at the band edges, which can increase the bandgap.

Optical Properties

The studies of the optical functions help to provide a deeper understanding of material properties and offer a clear perspective on their potential applications in optoelectronic devices. These functions are useful for investigating the energy band structure, impurity levels, excitons, localized defects, lattice vibrations, and certain magnetic excitations. In our research, we have employed first-principles calculations based on density functional theory to analyze the fundamental optical properties of both undoped and doped x: CdS (x = Mg, Ca, and Sr) crystals. From these spectra the optical constants, the real and imaginary dielectric constants, $\varepsilon_r(\omega)$ and $\varepsilon_I(\omega)$, refractive index n(ω), extinction coefficient, k(ω), absorption coefficient α(ω), reflectivity, R(ω), photoconductivity σ(ω), ands loss function L(ω) were investigated within the DFT framework with the GGA, and PBE as the exchange–correlation functional.

Dielectric Constants

The dielectric function is the response of the matter to the electromagnetic waves, which can be described in terms of time-dependent perturbations of the ground-state electronic levels. Electrons are excited and transited to the available unoccupied states due to the interactions of the electrons in the occupied states with the electric field of the photons. Spectra of the single electrons and plasmons occurred due to the optical transitions between the occupied and unoccupied states. The spectra resulting from these excitations can be described as a joint DOS between the valence and conduction bands. Using the electronic band structure, the linear response of the optical properties of the interested material can usually be depicted by the complex dielectric function $\varepsilon_I(\omega)$, which characterizes the linear response of a material to electromagnetic radiation and governs the propagation behavior of radiation in a medium given by[72]:

$$\varepsilon(\omega) = \varepsilon_r(\omega) + i\varepsilon_I(\omega) \tag{1}$$

where, $\varepsilon_r(\omega)$ and $\varepsilon_I(\omega)$ are real and imaginary parts of the dielectric function, respectively.

Figure 4(a) illustrates the calculated results of real dielectric constants $\varepsilon_r(\omega)$ for the pure and x:CdS (x = Mg, Ca, and Sr) 2 × 1 × 1 supercells. The calculated static dielectric constant $\varepsilon_r(0)$ is obtained at 4.56 for undoped CdS. The $\varepsilon_r(\omega)$ value increases slowly with the photon energy and achieves its maximum value 6.78 at the photon energy of 2.80 eV. The calculated static dielectric constants $\varepsilon_r(0)$ for the doped x:CdS (x = Mg, Ca, and Sr) are obtained as 5.14, 4.88, and 4.34, respectively. The prominent large peaks in the $\varepsilon_r(\omega)$ spectrum of x:CdS (x = Mg, Ca, and Sr) are 7.42, 6.95,

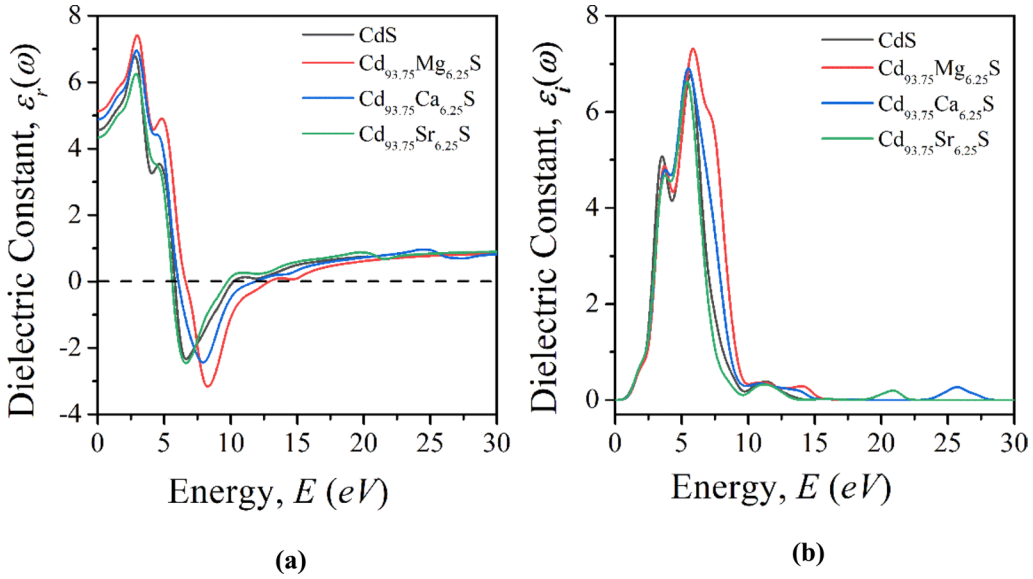

Fig. 4 (a) Real $\varepsilon_r(\omega)$ and (b) imaginary $\varepsilon_I(\omega)$ dielectric constant of undoped and x:CdS 2 × 1 × 1 supercells.

and 6.24, obtained at the corresponding photon energy of 2.95, 2.93, and 2.90 eV, respectively, revealing that the static dielectric constant increases greatly with Mg, Ca, and Sr doping on the Cd site. The prominent large peaks of x:CdS (x = Mg, Ca, and Sr) appear at higher energies compared to pure CdS; however, these peaks are observed to shift towards lower energy. This shifts in dielectric peaks towards lower energy upon Mg, Ca, and Sr doping in CdS 2 × 1 × 1 supercells may primarily be caused due to the modifications in the band structure, charge carrier concentration, increased bond lengths, lattice strain, and polarizability changes.[73]

The other peaks are obtained around the photon energy range 4 eV to n5 eV of 4.56 eV. These peaks are originated from the optical transition of the electrons or holes from the valence band to the empty conduction band. The first roots $\varepsilon_r(\omega)$ of pure and Mg-, Ca-, and Sr-doped CdS occurred at the energy ranges from 5.50 to 6.65 eV and of 5.70 eV, as well as the second roots are obtained at the energy ranges from 9.75 eV to 13.00 eV, respectively. The value of $\varepsilon_r(\omega)$ decreases sharply with increasing the photon energy after 3.00 eV. A valley-like nature is observed around photon energy ranges from 6.50 to 8.30 eV and the value then slowly increases to reach the second roots. Physically, the roots of $\varepsilon_r(\omega)$ are of great importance, as they can actually reveal plasmon energies where the electromagnetic wave cannot propagate because the value of $\varepsilon_r(\omega)$ becomes negative. As a result, the plasmon energies are roughly at 9.75–13.00 eV. The calculated values of the real dielectric constants are in good agreement with the reported results.[73]

Figure 4(b) presents the calculated imaginary dielectric constants, $\varepsilon_I(\omega)$, for the pure and x:CdS (x = Mg, Ca, and Sr) 2 × 1 × 1 supercells. The imaginary part of the dielectric function is computed using Fermi's Golden Rule[72,74]:

$$\varepsilon_I(\omega) = \frac{4\pi^2 e^2}{m^2\omega^2} \sum_{c,v} \int_{BZ} \frac{d^3k}{(2\pi)^3} |c,k|\hat{v}|v,k|^2 \delta\left(E_c(k) - E_v(k) - \hbar\omega\right) \tag{2}$$

where e is the elementary charge, m is the electron mass, ω is the photon frequency, c and v denote the conduction and valence band states, respectively, $E_c(k)$ and $E_v(k)$ are the energy eigenvalues of conduction and valence bands at wavevector k, $\hat{v}$ is the velocity operator, and $\delta\left(E_c(k) - E_v(k) - \hbar\omega\right)$ ensures that transitions occur at the correct energy difference.

The imaginary part of the dielectric function, $\varepsilon_I(\omega)$, represents the material's ability to absorb electromagnetic radiation at different photon energies $\hbar\omega$. It is directly related to interband electronic transitions, where photons excite electrons from occupied states in the valence band to unoccupied states in the conduction band. For pure and x:CdS (x = Mg, Ca, Sr) 2 × 1 × 1 supercells, the presence of large peaks around 5.7 eV in $\varepsilon_I(\omega)$ suggests that significant electronic transitions occur at this energy. These peaks correspond to the fundamental absorption edge and higher energy interband transitions. The high peaks indicate strong absorption, useful in optoelectronic applications such as photovoltaics and photodetectors[75]. The variation of $\varepsilon_I(\omega)$ with doping of Mg, Ca, and Sr can be attributed to changes in the electronic structure, such as bandgap modification and DOS near the Fermi level. The imaginary part also contributes to the energy dissipation in dielectric materials, affecting their performance in optical and electronic devices.

The absorption coefficient $\alpha(\omega)$ is directly related to $\epsilon_I(\omega)$ by[72]:

$$\alpha(\omega) = \frac{\omega}{cn(\omega)}\epsilon_I(\omega) \tag{3}$$

where c is the speed of light, and $n(\omega)$ is the refractive index of the material.

Refractive Index and Extinction Coefficient

The refractive index $n(\omega)$ describes how light propagates through a material and depends on the material's dielectric function. The behavior of $n(\omega)$ for undoped and x:CdS (x = Mg, Ca, Sr) 2 × 1 × 1 supercells are depicted in Fig. 5a. They are similar that of dielectric constants which can be obtained by the root of the dielectric constants, $n(\omega) = \sqrt{\varepsilon(\omega)}$.[72] The relationship between refractive index and dielectric function follows[72]:

$$n(\omega) = \frac{1}{\sqrt{2}}\left[\sqrt{\varepsilon_r^2(\omega) + \varepsilon_I^2(\omega)} + \varepsilon_r(\omega)\right]^{1/2} \tag{4}$$

The energy dependence of $n(\omega)$ follows from the Kramers–Kronig relationship, linking the real and imaginary parts of the dielectric function[72]:

$$\varepsilon_r(\omega) = 1 + \frac{2}{\pi}P\int_0^\infty \frac{\omega'\varepsilon_2(\omega')}{\omega'^2 - \omega^2}d\omega' \tag{5}$$

The peaks in the refractive index near 3.0 eV correspond to strong optical transitions due to interband electronic excitations, which likely corresponds to electronic excitations from deeper valence band states to conduction band states. It results from higher order interband transitions, excitonic effects, or doping-induced modifications in the electronic structure which suggests that significant light absorption and electron transitions occur in this region.

The dip or valley in the refractive index spectrum at ~ 9.5 eV indicates a reduced optical response, meaning that the material is less capable of interacting with light at this energy. This typically happens when the real part of the dielectric function $\varepsilon_r(\omega)$ changes sign or has a local minimum, leading to a lower refractive index. This can be applicable in photodetectors, solar cells, and LEDs, where a high refractive index at visible frequencies enhances light absorption and energy conversion efficiency, as well as for engineering materials with tailored optical responses.[76]

The extinction coefficient $k(\omega)$ is a fundamental optical property of a material that describes how much light is absorbed when it propagates through the material. It is part of the complex refractive index[72]:

$$n(\omega) = n(\omega) + ik(\omega) \tag{6}$$

This can also be written as[72]:

$$k(\omega) = \frac{1}{\sqrt{2}}\left[\sqrt{\varepsilon_r^2(\omega) + \varepsilon_I^2(\omega)} - \varepsilon_r(\omega)\right]^{1/2} \tag{7}$$

It is observed from Fig. 5b that the large peaks in $k(\omega)$ between 6.16 eV and 7.86 eV, which lie in the UV region, suggest that electrons are excited from the valence band to the conduction band, which means that the material strongly absorbs light at that frequency ω. At higher photon energies of 15 eV and beyond, the absorption decreases, which may due to the transition saturation as the available electrons have already

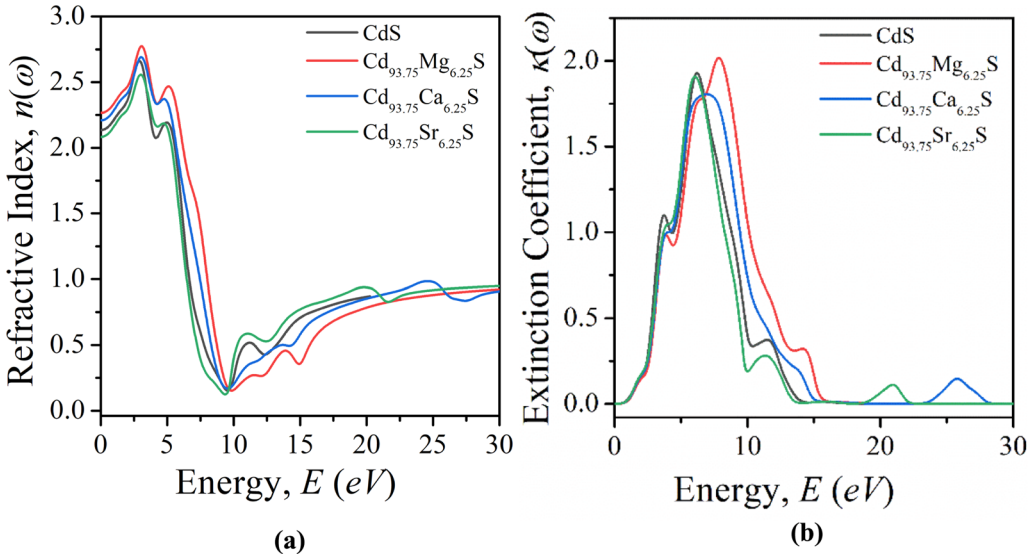

Fig. 5 (a) Refractive index n(ω) and (b) extinction coefficient k(ω) of undoped and x:CdS 2 × 1 × 1 supercells.

transitioned to higher states as well as reduced DOS. The electronic band structure may not support significant transitions at these energies. However, beyond 15 eV, the lower $k(\omega)$ reveals that the material is more transparent to that frequency.

Absorption Coefficient and Reflectivity

The absorption coefficient is crucial in determining the optical performance of CdS and doped CdS for various applications such as solar cells and photovoltaics, optoelectronic devices, transparent conductors.[77] High absorption in the UV-visible region improves the light-harvesting efficiency. This is defined as the fraction of the power absorbed in a unit length of the medium. If the beam is propagating in the x–direction, and the intensity (optical power per unit area) at position x is $I(x)$, then the decrease of the intensity in an incremental slice of thickness dx is given by[72]:

$$dI = -\alpha dx \times I(x) \tag{8}$$

The intensity of the electromagnetic radiation is directly related to the absorption coefficient $\alpha(\omega)$, which describes how the intensity of light decreases as it travels a distance,[72]:

$$I(x) = I_0 e^{-\alpha x} \tag{9}$$

where I_0 is the optical intensity at $x = 0$.

This can be integrated to obtain Beer's law,[72,78]:

$$\alpha(\omega) = \frac{4\pi k(\omega)}{\lambda} \tag{10}$$

where λ is the wavelength of light in vacuum.

The absorption coefficient is generally given by the equation. Alternatively, in terms of the imaginary part of the dielectric function $\varepsilon_I(\omega)$[72]:

$$\alpha(\omega) = \omega\sqrt{2}\left[\sqrt{\varepsilon_r^2(\omega) + \varepsilon_I^2(\omega)} - \varepsilon_r(\omega)\right]^{1/2} \tag{11}$$

The α(ω) describes how much light is absorbed by a material as a function of photon energy frequency (ω). It provides insights into the electronic transitions and optical properties of a material. Figure 6(a) displays the absorption coefficient, $\alpha(\omega)$, of undoped CdS and x:CdS (x = Mg, Ca, and Sr). A peak is seen close to the bandgap value, indicating the nature of direct optical transitions. It is observed that, when Mg, Ca, and Sr are introduced into the CdS 2 × 1 × 1 supercell, the absorption peaks increase in intensity and shift toward higher energy values. This shift is due to bandgap widening caused by the doping elements, as they modify the electronic structure of CdS. The large peaks observed around 6.42–8.17 eV correspond to strong interband transitions, indicating high optical absorption at these energies. This signifies that the material strongly absorbs light at that particular energy causes electronic transitions from the valence band to the conduction band. The absorption sharply decreases in the range of 13.80–15.90 eV, indicating that the material becomes more transparent in this region. The material then exhibits a transition from a strongly absorbing region to a more transparent one.

Reflectivity plays a vital role in analyzing the optical properties of semiconductors. High reflectivity in a specific energy range means that the material can reflect incident light efficiently, which is important for optical coatings,

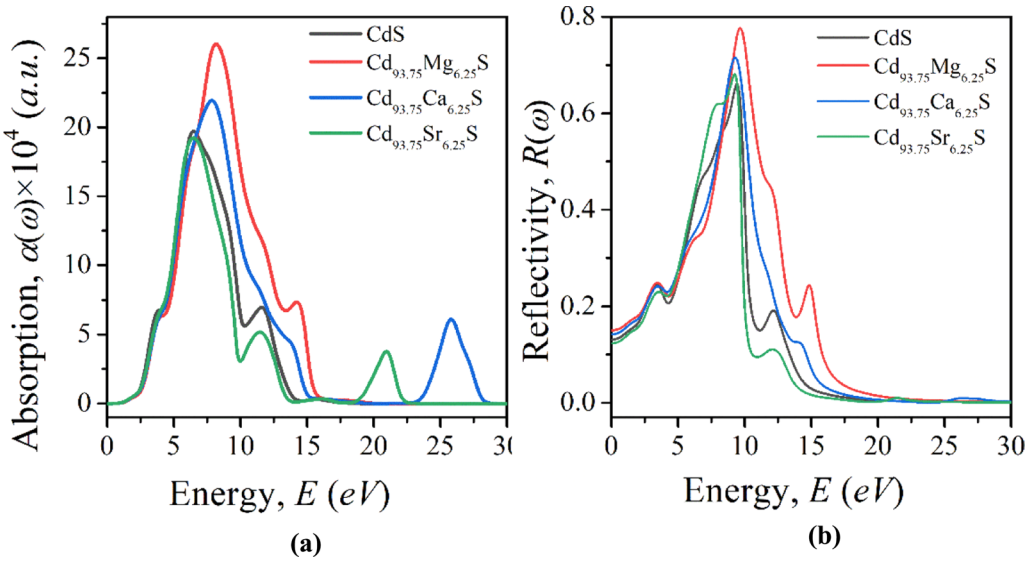

Fig. 6 (a) Absorption co-efficient α(ω) and reflectivity R(ω) of undoped and x:CdS 2 × 1 × 1 supercells.

photodetectors, and optoelectronic devices.[75] The reflectivity spectrum $R(\omega)$ provides insights into the optical response of materials as a function of frequency (ω).

The useful relationship connecting reflectivity and extinction coefficient,[72]:

$$R(\omega) = \left|\frac{n(\omega)-1}{n(\omega)+1}\right|^2 = \frac{\{n(\omega)-1\}^2 + k^2}{\{n(\omega)+1\}^2 + k^2} \tag{12}$$

Figure 6b represents the reflectivity spectrum, $R(\omega)$, of undoped CdS and x:CdS (x = Mg, Ca, and Sr) 2 × 1 × 1 supercells. Increases in reflectivity peaks with doping are observed due to the introduction of Mg, Ca, and Sr into the CdS, showing that they enhance the reflectivity peaks, indicating stronger optical response in the UV range. This enhancement occurs due to changes in the electronic structure and dielectric function of the material. However, the peaks are observed to shift towards the higher energy suggesting a bandgap widening, which is a typical consequence of semiconductor doping. The increased bandgap results from the modification of the electronic states due to the substitution of Cd with Mg, Ca, and Sr. The highest peaks occurring around 9.5 eV indicate a strong interaction of incident photons with the material, leading to high reflectivity, corresponding to interband transitions, where electrons move from the valence band to the conduction band. Additionally, the spectrum is found to decrease sharply at around 14.5–20 eV. This drop-in reflectivity at higher photon energies suggests that the material starts absorbing more light instead of reflecting it. This could be due to increased electronic excitations that allow photons to penetrate rather than be reflected. These suggest that doping of CdS with Mg, Ca, and Sr modifies the reflectivity properties, potentially improving optoelectronic properties as well as enhancing the optical performance for UV and deep-UV applications, and may be recommended for the use in solar cells, LEDs, and photodetectors.[7,44]

Photoconductivity and Loss Function

Photoconductivity $\sigma(\omega)$ represents the material's response to incident light, where photons excite electrons from the valence band to the conduction band, leading to an increase in electrical conductivity. The changes in photoconductivity due to doping affect carrier recombination rates and mobility, which is crucial for designing high-performance electronic and optoelectronic devices. The photoconductivity is directly proportional to the absorption component of the dielectric function[72,78]:

$$\sigma(\omega) = \frac{\omega\varepsilon_0\varepsilon_I(\omega)}{4\pi} \tag{13}$$

where ε_0 is the permittivity of free space.

Also, we can calculate the optical conductivity using [79]:

$$\sigma(\omega) = \frac{\alpha nc}{4\pi} \tag{14}$$

The optical conductivity, $\sigma(\omega)$, of undoped CdS and x:CdS (x = Mg, Ca, Sr) is displayed in Fig. 7a. The observed behavior of the photoconductivity peaks in CdS 2 × 1 × 1 supercells with Mg, Ca, and Sr doping can be understood as follows. The photoconductivity starts rising around the bandgap energy because photons with energy equal to or greater than the bandgap excite electrons across the

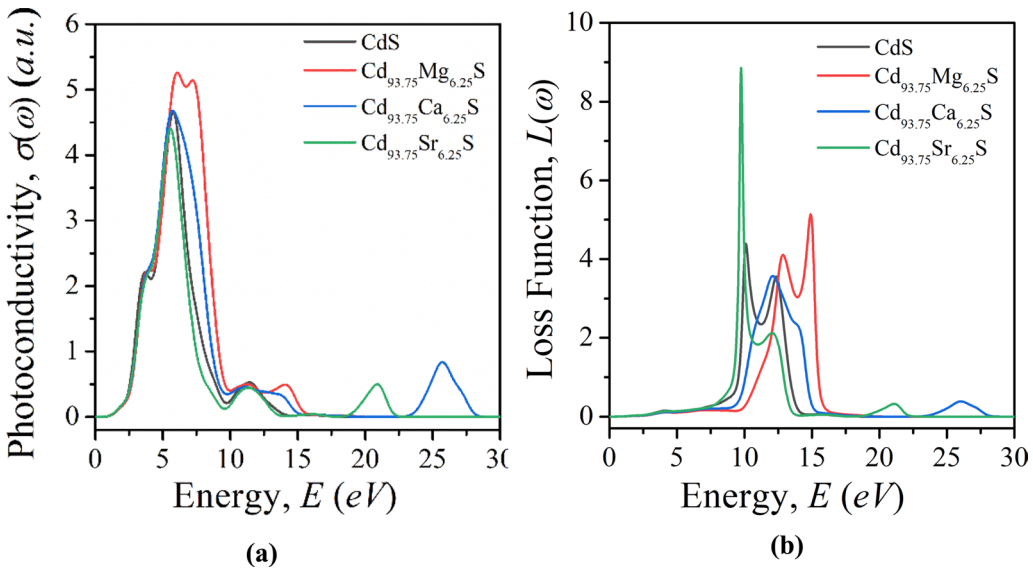

Fig. 7 (a) Photoconductivity σ(ω) and (b) loss function L(ω) of undoped and x:CdS 2 × 1 × 1 supercells.

gap. When CdS is doped with Mg, Ca, or Sr, the bandgap changed slightly due to modifications in the electronic structure, shifting the photoconductivity onset slightly, indicating that dopant atoms influence the material's absorption edge and carrier excitation.

A high photoconductivity peaks around the electromagnetic energy range of 5.50–6.05 eV, which suggests strong optical transitions between electronic states. These peaks correspond to interband transitions where electrons are excited to available higher conduction band states, leading to significant charge carrier generation. The sharp decrease of the photoconductivity spectrum at high energy ~ 9.70 eV suggests that the density of available electronic states reduces beyond this energy. This may occur due to the strong absorption leading to reduced free carrier movement at higher photon energies. It might also be associated with the onset of core electron excitations, where conduction band transitions become less dominant. Due to its strong photoconductive response in the visible and UV regions, CdS doping with Mg, Ca, or Sr has tailored the bandgap and carrier dynamics, improving efficiency, and proposing the usefulness of these compounds in optoelectronic applications such as photodetectors and solar cells.[64,80]

The dielectric loss function $L(\omega)$ describes the energy dissipation in a material when subjected to an oscillating electric field. It provides insights into how a material interacts with electromagnetic waves and is crucial for understanding optical and plasmonic properties. It is vital in analyzing plasmonic excitations, which are essential in optoelectronic and photonic applications. The dielectric loss function $L(\omega)$ is directly related to the dielectric constant (or complex dielectric function), which consists of a real part $\varepsilon_r(\omega)$ and an imaginary part $\varepsilon_I(\omega)$[32,72]:

$$L(\omega) = Im\frac{-1}{\varepsilon(\omega)} = \frac{\varepsilon_I(\omega)}{\varepsilon_r^2(\omega) + \varepsilon_I^2(\omega)} \tag{15}$$

Plasmon frequencies correspond to the condition where the real part of the dielectric function $\varepsilon_r(\omega)$ approaches zero while $\varepsilon_I(\omega)$ remains small[72]:

$$\varepsilon_r(\omega_p) \approx 0 \tag{16}$$

At the frequency ω_p, the material exhibits a strong collective oscillation of charge carriers, leading to a peak in $L(\omega)$. The plasmon frequency depends on the free carrier concentration and is influenced by doping. The peaks in $L(\omega)$ are associated with plasmon resonances, which occur when the collective oscillations of free or bound charge carriers interact strongly with incident radiation.

Figure 7b show the dielectric loss function $L(\omega)$ of undoped CdS and x:CdS (x = Mg, Ca, Sr). For the CdS $2 \times 1 \times 1$ supercell, the observed dielectric loss peaks are obtained 10.07, 14.92, 12.15, and 9.73 eV for pure and Mg-, Ca-, and Sr-doped CdS, respectively. This reveals that the doping modifies the electronic band structure, shifting the energy levels involved in plasmonic excitations. Different dopants contribute different numbers of free carriers, affecting the plasmon frequency. Mg, Ca, and Sr have different atomic sizes and electronegativities, leading to variations in the dielectric response. The introduction of dopants induces local lattice distortions, affecting charge carrier dynamics and modifying optical properties.[81]Mg introduces a more significant shift in the conduction band states, leading to a stronger plasmonic resonance at 14.92 eV. The other dopants (Ca, Sr) induce moderate shifts, leading to peaks at lower energies.[81]

Conclusions

This study presents a detailed computational analysis of the effects of Mg, Ca, and Sr doping on the structural, electronic, and optical properties of CdS using DFT-based CASTEP calculations. The findings reveal that substituting Cd with these alkaline earth metals introduces significant modifications in the lattice structure, electronic bandgap, and optical behavior, thereby enhancing the material's optoelectronic performance.

Structural analysis indicates that doping alters the lattice parameters and bond lengths, with Sr incorporation causing the largest expansion due to its larger ionic radius. These structural changes influence the electronic properties, as evidenced by the band structure calculations. The results confirm that all three dopants contribute to bandgap widening, a consequence of the Burstein–Moss effect, with Ca doping yielding the most pronounced increase. The increase in the bandgap of Mg-, Ca-, and Sr-doped CdS is primarily due to reduced covalency, minimal impurity states near the Fermi level, changes in the bond nature, and slight lattice distortions. The absence of significant defect states prevents bandgap narrowing, leading to a net widening of the bandgap. This widening improves charge carrier mobility and reduces electron–hole recombination, making the doped CdS a more efficient material for high-performance optoelectronic applications.

The optical property analysis further validates the potential of doping in optimizing CdS. The dielectric function results show that doping enhances the material's ability to interact with light, leading to increased absorption in the ultraviolet-visible range. The refractive index and extinction coefficient calculations indicate that Mg, Ca, and Sr doping improve light propagation and absorption, crucial for photovoltaic and photodetector applications. Additionally, photoconductivity analysis reveals that Mg doping significantly enhances carrier generation, suggesting its suitability for devices requiring high photoconductive responses.

The dielectric loss function provides crucial insights into the optical and plasmonic properties of doped CdS. The observed deviations in peak positions arise due to electronic structure modifications, carrier density variations, and lattice distortions induced by dopants. Mg doping significantly enhances the loss function peak, suggesting a stronger plasmonic response, whereas Sr-doped CdS exhibits a lower energy peak due to its electronic influence on the material.

A key finding is that different dopants exhibit distinct advantages: Ca doping leads to the most substantial bandgap increase, Sr doping maintains balanced electronic and optical improvements, while Mg doping enhances photoconductivity. These insights suggest that doping CdS with alkaline earth metals can be a viable strategy for optimizing its optoelectronic properties.

Overall, this study provides a theoretical foundation for experimental research on doped CdS materials. Future work could focus on co-doping strategies, defect engineering, and optimizing doping concentrations to further enhance CdS's performance for real-world applications, including solar cells, LEDs, and photodetectors. The insights gained from this study contribute to the advancement of CdS-based semiconductors for next-generation optoelectronic devices.

Acknowledgments Authors are thankful to the Department of Physics, Uttara University, Holding 77, Beribadh Road, Turag, Uttara, Dhaka-1230, Bangladesh and the Department of Physics, Begum Rokeya University, Rangpur, Rangpur 5400, Bangladesh for their full support and providing Computer Lab facilities to investigate the study.

Author Contributions Mosfiqur Rahman and Mst. Afroza Akter designed the study, interpreted the data, and wrote the manuscript. Md. Mamunur Roshid, and Md. Monirul Haq helped with the theoretical study, analyzed data, and wrote the manuscript.

Funding This research received no external funding.

Data availability Relevant data from this study are available from the corresponding author upon a reasonable request.

Conflict of interest The authors declare that they have no conflicts of interest.

References

1. C. Li, Y. Zhang, G. Hao, and F. Wang, Effect of Cu doping on the electronic structure, magnetic and optical properties of GaN/ZnS heterojunctions: a first-principles study. *Eur. Phys. J. Appl. Phys.* 99, 26 (2024).
2. J. Wong-Leung, I. Yang, Z. Li, S.K. Karuturi, L. Fu, H.H. Tan, and C. Jagadish, Engineering III–V semiconductor nanowires for device applications. *Adv. Mater.* 32(18), 1904359 (2020).
3. A.I. Mikhailov, V.F. Kabanov, I.A. Gorbachev, and E.G. Glukhovsky, Study of the properties of II–VI and III–V semiconductor quantum dots. *Semiconductors* 52(6), 750–754 (2018).
4. M. Rahman, M. Kamruzzaman, J.A. Zapien, R. Afrose, T.K. Anam, M.N.H. Liton, M.A. Helal, and M.K.R. Khan, Conversion of n-type to p-type conductivity in ZnO by incorporation of Ag and Ag-Li. *Mater. Today Commun.* 33, 104278 (2022).
5. T. Geremew and T. Abza, Microstructural and optical characterization of heterostructures of ZnS/CdS and CdS/ZnS synthesized by chemical bath deposition method. *Adv. Mater. Sci. Eng.* 2020(1), 1401689 (2020).
6. M. Riju Khandaker, M. Kamruzzaman, R. Afrose, M. Rahman, M.K. Khan, M.N. Liton, M.A. Helal, T.K. Anam, and M.M. Rahman, Enhanced optical properties of FeS_2 Using Ni@ Cu doping and characterization of the structural and chemical compositions for solar cell applications. *Crystallogr. Rep.* 65, 968–979 (2020).
7. M. Gandouzi, H. Alshammary, Z.R. Khan, A.S. Alshammari, and F. Hedhili, Experimental and DFT studies of structural and optoelectronic properties of CdS, Zn doped CdS, and (Zn-Ni) co-doping CdS nanomaterials. *Phys. Scr.* 99(6), 065935 (2024).
8. A. Abuhusain, F. Abdulaziz, M. Gandouzi, A.S. Alshammari, M. Bouzidi, M. Mohamed, and Z.R. Khan, Experimental and theoretical investigation of pure and (Co, Sr) co-doped CdS system for optoelectronics applications: A quantitative comparison. *Physica B* 655, 414735 (2023).
9. K.E. Nieto-Zepeda, J.G. Quiñones-Galván, K. Rodríguez-Rosales, A. Guillén-Cervantes, J. Santos-Cruz, O. Zelaya-Ángel, and F. de Moure-Flores, Optoelectronic properties of Cl and F doped CdS thin films grown by chemical bath deposition. *Optik* 226, 166004 (2021).
10. M. Kamruzzaman, J.A. Zapien, R. Afrose, T.K. Anam, M. Rahman, M.N.H. Liton, M.A. Helal, M.K.R. Khan, and A.A. Emmanuel, A comparative study of Ag doping effects on the electronic, optical, carrier conversion, photocatalytic and electrical properties of MoS_2. *Mater. Sci. Eng. B* 273, 115442 (2021).
11. A. Alam, S. Kumar, and D.K. Singh, Cadmium sulphide thin films deposition and characterization for device applications. *Mater. Today: Proc.* 62, 6102–6106 (2022).
12. A. El-Shaer, S. Ezzat, M.A. Habib, O.K. Alduaij, T.M. Meaz, and S.A. El-Attar, Influence of deposition time on structural, morphological, and optical properties of CdS thin films grown by low-cost chemical bath deposition. *Crystals* 13(5), 788 (2023).
13. K.B.A. Ahmed, M.R.C. Raja, S.K. Mahapatra, and V. Anbazhagan, Interaction of cadmium sulfide quantum dots with jacalin for specific recognition of cancer cells. *J. Lumin.* 182, 283–288 (2017).
14. P. Wu, and X.P. Yan, Doped quantum dots for chemo/biosensing and bioimaging. *Chem. Soc. Rev.* 42(12), 5489–5521 (2013).
15. O.Y. Tkacheva, Thermal expansion of alkali and alkaline earth halides in solid and molten states. *Electrochem. Mater. Technol.* 4(1), 20254049 (2025).
16. Y. Zhang, L. Zhou, and J.F. Mao, Inverse piezoelectric and trap effects with temperature dependence in AlGaN/GaN HEMTs under narrowband microwave pulses. *IEEE Trans. Electromagn. Compat.* 65(3), 794–803 (2023).
17. S.A. Vanalakar, V.L. Patil, S.M. Patil, S.P. Deshmukh, P.S. Patil, and J.H. Kim, Chemical and gas sensing property tuning of cadmium sulfide thin films. *Mater. Sci. Eng. B* 282, 115787 (2022).
18. M. Kaleli, Effect of sulphurization and Al doping on Cd0. 25Zn0. 75S thin films deposited by ultrasonic spray pyrolysis technique. *Optik* 207, 163781 (2020).
19. K. Erturk, S. Isik, O. Aras, and Y. Kaya, Investigation of structural, spectral, optical and nonlinear optical properties of nanocrystal CdS: electrodeposition and quantum mechanical studies. *Optik* 243, 167469 (2021).
20. J. Ziembicki, P. Scharoch, M.P. Polak, M. Wiśniewski, and R. Kudrawiec, Electronic and structural properties of group IV materials and their polytypes. *J. Appl. Phys.* (2024). https://doi.org/10.1063/5.0229832.
21. G.C. Righini, C. Armellini, M. Ferrari, A. Carlotto, A. Carpentiero, A. Chiappini, A. Chiasera, A. Lukowiak, T.N. Tran, and

S. Varas, Sol–gel photonic glasses: from material to application. *Materials* 16(7), 2724 (2023).
22. M. Seol, H. Kim, W. Kim, and K. Yong, Highly efficient photoelectrochemical hydrogen generation using a ZnO nanowire array and a CdSe/CdS co-sensitizer. *Electrochem. Commun.* 12(10), 1416–1418 (2010).
23. M.H. Mia, M.A. Khatun, and M. Rahman, Ti2PTe2 chalcogenide: A comprehensive DFT study on physical properties. *Next Mater.* 7, 100434 (2025).
24. Y. Al-Douri, J.H. Waheb, M. Ameri, R. Khenata, A. Bouhemadou, and A.H. Reshak, Morphology, analysis and properties studies of CdS nanostructures under thiourea concentration effect for photovoltaic applications. *Int. J. Electrochem. Sci.* 8(8), 10688–10696 (2013).
25. C. Ferekides, D. Marinskiy, and D. L. Morel, CdS: Characterization and recent advances in CdTe solar cell performance. In Conference Record of the Twenty Sixth IEEE Photovoltaic Specialists Conference (1997) (pp. 339-342). IEEE.
26. M.A. Sayed, M. Kamruzzaman, M.N.H. Liton, M.A. Helal, and M. Rahman, Investigation of site dependent donor-acceptor (Al-N) doping effect into ZnO for optoelectronic applications. *J. Sci. Res.* 16(1), 171–186 (2024). https://doi.org/10.3329/jsr.v16i1.66310.
27. R. Afrose, M. Kamruzzaman, M.N.H. Liton, M.A. Helal, M.K.R. Khan, M. Rahman, and T.K. Anam, Synthesis and characterization of Zn 1 0 0–x Li x O and Zn 1 0 0–x− y Li x Cu y O thin films for electronic and optoelectronic applications. *Int. J. Mod. Phys. B* 33(23), 1950257 (2019).
28. R. Zhao, P. Wang, B.B. Yao, T.T. Hu, T.Y. Yang, B.X. Xiao, S.M. Wang, C.H. Xiao, and M.Z. Zhang, Co effect on zinc blende–rocksalt phase transition in CdS nanocrystals. *RSC Adv.* 5(23), 17582–17587 (2015).
29. M.A. Abdulsattar, B.B. Kadhim, and A.M. Ali, Effect of temperature and pressure on electronic and spectroscopic properties of CdS wurtzoid molecule: A DFT study. *Optik* 188, 126–132 (2019).
30. M.J.I. Khan, M.N. Usmani, Z. Kanwal, and P. Akhtar, Novel substitutional effects on optical properties of Cds: Co system (A theoretical study). *Optik* 156, 817–824 (2018).
31. M.J.I. Khan, and Z. Kanwal, First principle calculations of optical properties of CdS: Al system (A DFT+ U study). *Mater. Res Exp.* 6(3), 035905 (2018).
32. M. Kamruzzaman, J.A. Zapien, M. Rahman, R. Afrose, T.K. Anam, M.N.H. Liton, M.A. Helal, and M.K.R. Khan, Effects of p-type (Ag, Cu) dopant on the electronic, optical and photocatalytic properties of MoS2, and impact on Au/Mo100-x-yAgxCuyS_2 performance. *J. Alloy. Compd.* 863, 158366 (2021).
33. B.P. Singh, R. Kumar, A. Kumar, and R.C. Tyagi, Vacuum deposition of stoichiometric crystalline PbS films: the effect of sulfurizing environment during deposition. *Mater. Res. Exp.* 2(10), 106401 (2015).
34. M.S. Khan, A. Aziz, S.A. Rahman, and Z.R. Khan, Spectroscopic studies of sol–gel grown CdS nanocrystalline thin films for optoelectronic devices. *Mater. Sci. Semicond. Process.* 16(6), 1894–1898 (2013).
35. J. Trajić, M. Gilić, N. Romčević, M. Romčević, G. Stanišić, B. Hadžić, M. Petrović, and Y.S. Yahia, Raman spectroscopy of optical properties in CdS thin films. *Sci. Sinter.* 47(2), 145–152 (2015).
36. S.M. AL-Jawad, N.J. Imran, and K.H. Aboud, Synthesis and characterization of Mn: CdS nanoflower thin films prepared by hydrothermal method for photocatalytic activity. *J. Sol-Gel Sci. Technol.* 100, 423–439 (2021).
37. S.U. Shaikh, D.J. Desale, F.Y. Siddiqui, A. Ghosh, R.B. Birajadar, A.V. Ghule, and R. Sharma, Effects of air annealing on CdS quantum dots thin film grown at room temperature by CBD technique intended for photosensor applications. *Mater. Res. Bull.* 47(11), 3440–3444 (2012).
38. K. Prabakar, H. Seo, M. Son, and H. Kim, CdS quantum dots sensitized TiO2 photoelectrodes. *Mater. Chem. Phys.* 117(1), 26–28 (2009).
39. Z.R. Khan, A.S. Alshammari, M. Shkir, V. Ganesh, S. AlFaify, and Munirah., Enhancement in the photoluminescence, linear and third order nonlinear optical properties of nanostructured Na-CdS thin films for optoelectronic applications. *J. Nanopart. Res.* 22, 1–16 (2020).
40. T. Garmim, E. Bouabdalli, L. Soussi, Z. El Jouad, R. Mghaiouini, A. Louardi, B. Hartiti, M.E. Jouad, and M. Monkade, Opto-electrical properties of Ni and Mg co-doped CdS thin films prepared by spin coating technique. *Phys. Scr.* 96(4), 045813 (2021).
41. Z.R. Khan, M. Munirah, A.S. Shkir, V. Alshammari, S. Ganesh, and M.G. AlFaify, Structural, linear and third order nonlinear optical properties of sol-gel grown Ag-CdS nanocrystalline thin films. *J. Electron. Mater.* 48(2), 1122–1132 (2019). https://doi.org/10.1007/s11664-018-6832-2.
42. M. Gunasekaran and P. Seenuvasakumaran, Structural and optical properties of CdS & Pb doped CdS thin films coated by spin coating technique. *Mater. Today: Proc.* 49, 2707–2711 (2022).
43. M. Anbarasi, V.S. Nagarethinam, R. Baskaran, and V. Narasimman, Studies on the structural, morphological and optoelectrical properties of spray deposited CdS: Pb thin films. *Pacific Sci. Rev. A: Nat. Sci. Eng.* 18(1), 72–77 (2016).
44. M.J.I. Khan, Z. Kanwal, M.N. Usmani, M. Zeeshan, and M. Yousaf, An insight into optical properties of Pb: CdS system (a theoretical study). *Mater. Res. Exp.* 6(6), 065904 (2019).
45. Z.K. Heiba, M.B. Mohamed, and S.I. Ahmed, Optical and electronic correlation in Mg-doped nano cadmium sulfide. *Opt. Quant. Electron.* 53, 1–17 (2021).
46. C. Feng, Z. Chen, J. Jing, M. Sun, H. Tong, and J. Hou, Band structure and enhanced photocatalytic degradation performance of Mg-doped CdS nanorods. *Phys. B* 594, 412363 (2020).
47. S. Chakraborty and M. Pal, Improved sensitivity of CdS nanoparticles by virtue of calcium doping: promising candidate for monitoring alcohol in exhale human breath. *Mater. Des.* 126, 18–28 (2017).
48. M. Banerjee, A. Sharma, and L. Chongad, Effect of doping Pb on the structural and optical properties of nanostructured CdS films. *Res. J. Recent Sci. ISSN* 2277, 2502 (2013).
49. R. Gutiérrez, O. Portillo, M. Chávez, H. Juarez, M. Pacio, L. Chaltel, M. Zamora, M. Lazcano, E. Rubio, and G. Hernandez, Optical and structural properties of CdS: Pb^2+ nanocrystals. *Revista mexicana de física* 61(4), 312–322 (2015).
50. H.S.A. Umaili, Structural and optical properties of nanocrystalline Pb1–xCdxS thin films prepared by chemical bath deposition. *Appl. Phys. Res.* 4(3), 75–82 (2012).
51. I.F. Ertis and I. Boz, Synthesis and characterization of metal-doped (Ni Co, Ce, Sb) CdS catalysts and their use in methylene blue degradation under visible light irradiation. *Modern Res. Catal.* 6(01), 1 (2017).
52. J.P. Perdew and A. Zunger, Self-interaction correction to density-functional approximations for many-electron systems. *Phys. Rev. B* 23(10), 5048 (1981).
53. J.P. Perdew, K. Burke, and M. Ernzerhof, Generalized gradient approximation made simple. *Phys. Rev. Lett.* 77(18), 3865 (1996).
54. S.L. Dudarev, G.A. Botton, S.Y. Savrasov, C.J. Humphreys, and A.P. Sutton, Electron-energy-loss spectra and the structural stability of nickel oxide: An LSDA+ U study. *Phys. Rev. B* 57(3), 1505 (1998).
55. D. Fritsch, B.J. Morgan, and A. Walsh, Self-consistent hybrid functional calculations: implications for structural, electronic, and optical properties of oxide semiconductors. *Nanoscale Res. Lett.* 12, 1–7 (2017).

56. P. Giannozzi, O. Baseggio, P. Bonfà, D. Brunato, R. Car, I. Carnimeo, C. Cavazzoni, S. de Gironcoli, P. Delugas, F.F. Ruffino, A. Ferretti, N. Marzari, I. Timrov, A. Urru, and S. Baroni, Quantum ESPRESSO toward the exascale. *J. Chem. Phys.* (2020). https://doi.org/10.1063/5.0005082.
57. Y. Liu, J. Lian, M. Zhao, Y. Wang, M. Li, and H. Song, The effect of defects on Cu-doped CdS: a first-principles study. *Europhys. Lett.* 117(5), 57007 (2017).
58. X.D. Liu, and T. Xing, First-principles calculations of electronic structures and optical properties of group-IIIA elements doped wurtzite CdS. *Solid State Commun.* 187, 72–76 (2014).
59. M. Boudjelal, A. Belfedal, B. Bouadjemi, T. Lantri, R. Bentata, M. Batouche, and R. Khenata, Ferromagnetic half-semiconductor (HSC) gaps in co-doped CdS: Ab-initio study. *Chin. J. Phys.* 61, 155–165 (2019).
60. W. Sukkabot, Theoretical investigation of electronic and magnetic optical properties of CdS doped and co doped with transition metals (Mn, Fe, and Cu): spin density functional theory. *IEEE Trans. Magn.* 56(9), 1–6 (2020).
61. A. Nabi, The electronic and the magnetic properties of Mn doped wurtzite CdS: First-principles calculations. *Comput. Mater. Sci.* 112, 210–218 (2016).
62. S.J. Clark, M.D. Segall, C.J. Pickard, P.J. Hasnip, M.I.J. Probert, K. Refson, and M.C. Payne, First principles methods using CASTEP. *Zeitschrift für Kristallographie – Cryst. Mater.* 220(5–6), 567–570 (2005). https://doi.org/10.1524/zkri.220.5.567.65075.
63. N.A. Noor, W. Tahir, F. Aslam, and A. Shaukat, Ab initio study of structural, electronic and optical properties of Be-doped CdS, CdSe and CdTe compounds. *Physica B* 407(6), 943–952 (2012).
64. N. Ahmed, A. Nabi, J. Nisar, M. Tariq, M.A. Javid, and M.H. Nasim, First principle calculations of electronic and magnetic properties of Mn-doped CdS (zinc blende): a theoretical study. *Mater. Sci.-Pol.* 35(3), 479–485 (2017).
65. M. Anbarasi, V.S. Nagarethinam, K. Usharani, S. Balamurugan, D. Prabha, M. Suganya, J. Srivind, and A.R. Balu, Influence of strontium doping level on the magnetic properties of CdS thin films. *J. Mater. Sci. Mater. Electron.* 28, 14848–14854 (2017).
66. V. Ribić, A. Rečnik, M. Komelj, A. Kokalj, Z. Branković, M. Zlatović, and G. Branković, New inversion boundary structure in Sb-doped ZnO predicted by DFT calculations and confirmed by experimental HRTEM. *Acta Mater.* 199, 633–648 (2020).
67. C. Feng, Z. Chen, W. Li, F. Zhang, X. Li, L. Xu, and M. Sun, First-principle calculation of the electronic structures and optical properties of the metallic and nonmetallic elements-doped ZnO on the basis of photocatalysis. *Physica B* 555, 53–60 (2019).
68. E. Burstein, Anomalous optical absorption limit in InSb. *Phys. Rev.* 93(3), 632 (1954).
69. T.S. Moss, The interpretation of the properties of indium antimonide. *Proc. Phys. Soc. Sect. B* 67(10), 775–782 (1954). https://doi.org/10.1088/0370-1301/67/10/306.
70. S.J. Gnanamuthu, S.J. Jeyakumar, I.K. Punithavathy, P.J. Prabhakar, M. Suganya, K. Usharani, and A.R. Balu, Properties of spray deposited nano needle structured Cu-doped Sn2S3 thin films towards photovoltaic applications. *Optik* 127(8), 3999–4003 (2016).
71. J.C. Wu, J. Zheng, P. Wu, and R. Xu, Study of native defects and transition-metal (Mn, Fe Co, and Ni) doping in a zinc-blende CdS photocatalyst by DFT and hybrid DFT calculations. *J. Phys. Chem. C* 115(13), 5675–5682 (2011).
72. M. Fox, *Optical properties of solids*, Vol. 3 (Oxford: Oxford University Press, 2010).
73. Y.X. Han, C.L. Yang, Y.T. Sun, M.S. Wang, and X.G. Ma, The novel optical properties of CdS caused by concentration of impurity Co. *J. Alloy. Compd.* 585, 503–509 (2014).
74. G.Y. Guo, K.C. Chu, D.S. Wang, and C.G. Duan, Linear and nonlinear optical properties of carbon nanotubes from first-principles calculations. *Phys. Rev. B* 69(20), 205416 (2004).
75. L. Zhang, J. Ran, S.Z. Qiao, and M. Jaroniec, Characterization of semiconductor photocatalysts. *Chem. Soc. Rev.* 48(20), 5184–5206 (2019).
76. W. Wang and L. Qi, Light management with patterned micro-and nanostructure arrays for photocatalysis, photovoltaics, and optoelectronic and optical devices. *Adv. Func. Mater.* 29(25), 1807275 (2019).
77. M.J.I. Khan and Z. Kanwal, Investigation of optical properties of CdS for various Na concentrations for nonlinear optical applications (A DFT study). *Optik* 193, 162985 (2019).
78. M. Kaneko, V. Nandal, K. Yamashita, and K. Seki, Use of energy bandgap adjustment when simulating optical properties to maintain correct energy dissipation: Application to Ruddlesden–Popper oxysulfides. *AIP Adv.* (2024). https://doi.org/10.1063/5.0205825.
79. I.M. El Radaf, T.A. Hameed, and I.S. Yahia, Synthesis and characterization of F-doped CdS thin films by spray pyrolysis for photovoltaic applications. *Mater. Res. Exp.* 5(6), 066416 (2018).
80. J. Zhang, S. Wageh, A. Al-Ghamdi, and J. Yu, New understanding on the different photocatalytic activity of wurtzite and zinc-blende CdS. *Appl. Catal. B* 192, 101–107 (2016).
81. Benlakhdar, F. (2024). Contribution to the study of the doping effect on the characteristics of some semiconductor compounds, theoretical study (Doctoral dissertation).